PIV measurements of the structure of wing-tip trailing vortices and their comparison with theoretical models

Carlos del Pino[1], Luis Parras[2], Mario Felli[3], Ramón Fernandez-Feria[4]

1: ETS de Ingenieros Industriales, University of Málaga, Spain, cpino@uma.es
2: ETS de Ingenieros Industriales, University of Málaga, Spain, lparras@uma.es
3: Cavitation and Propulsion Laboratory, INSEAN, Roma, Italy, m.felli@insean.it
4: ETS de Ingenieros Industriales, University of Málaga, Spain, ramon.fernandez@uma.es

Abstract The velocity field of the trailing vortex behind a wing at different angles of attack has been measured through the Stereo PIV technique in a water tunnel for Reynolds numbers between 20000 and 40000, and for several distances to the wing tip. After filtering out the vortex meandering, the radial profiles of the axial and the azimuthal velocity components and, especially, the radial profiles of the vorticity, were fitted to several theoretical models for trailing vortices. We take into account the axial variation of these profiles from just a fraction of the wing chord to more than ten chords. Both the radial profiles and their streamwise variation are shown to fit quite well to Moore and Saffman's (1973) model (Proc R Soc Lond A 333:491-508).

1. Introduction

The precise knowledge of the dynamics of trailing vortices in the wake behind commercial aircrafts and their control are relevant issues in civil aviation, for these vortices strongly affect the frequencies of taking off and landing of aircrafts in an airport (e.g., Spalart 1998, Gertz et al 2002). Many recent numerical and experimental researches have investigated the behavior of aircraft vortices, aiming at their characterization and the search for means of reducing the associated hazard (e.g., Jacquin et al 2001, Gertz et al 2005, Allen and Breitsamter 2009, Deniau and Nybelen 2010). Within these investigations, one of the main lines of research is about the role of vortex instabilities on wake decay (e.g., Fabre and Jacquin 2004a-b, Le Dizès and Fabre 2007, Parras and Fernandez-Feria 2007, Fabre and Le Dizès 2008). But these works also show that the hydrodynamic stability predictions strongly depend on the detailed structure used as base flow models for these trailing vortices, particularly on the sometimes neglected axial flow. In this scenario, the accurate experimental survey of trailing vortices behind aircraft wings, especially near the tip, and, in particular, the characterization of the downstream evolution of their velocity fields represent relevant issues for the assessment of the best theoretical models. Such models reveal suitable for the stability analysis of the trailing wake vortices which may be used to predict their dynamics and decay as well as to control them. This is the main objective of the present work.

Early experimental measurements of wing tip vortices were undertaken by Olsen (1971), who used flow visualization techniques, and by Baker et al (1974), which utilized the, by that time just developed, technique of Laser Doppler Anemometry (LDA). This technique was also recently used by Jacquin et al (2001) to measure the near field structure of aircraft wakes. Relevant experimental measurements of isolated wing tip vortices, using LDA and/or Particle Image Velocimetry (PIV) techniques, were made by Devenport et al (1996) and by Roy and Leweke (2005). These authors fitted their experimental results to a q-vortex model and to a two-core scales vortex model, respectively. However, these measurements were taken at fixed axial locations of the vortex, without any attempt to obtain the axial variation of the velocity field, which constitutes one of the main objectives of the present work. The knowledge of this axial dependence of the velocity

components is important to decide about the family of vortex models fitting the experimental measurements.

One of the main difficulties of measuring the velocity field in a wing-tip vortex is the *meandering* phenomenon, or random fluctuation of the vortex centerline. This meandering is quite significant a few chords downstream the wing, but it is less pronounced within a chord of the trailing edge. A consequence of the meandering (or *wandering*) phenomenon is that vortices measured by static measuring techniques appear to be more diffuse than in reality, so that a correction method is needed (Devenport et al 1996, Iungo et al 2009). Recent work on transient energy growth through an optimal perturbation analysis and a stochastic forcing analysis (Fontane et al 2008) shows that the very long wavelength observed in the meandering of trailing vortices can be explained by a resonant excitation due to noise located outside of the vortex core (Fabre et al 2008). Therefore, vortices are very sensitive to even very small intrusive probes, and only non-intrusive techniques such as LDA or PIV yield consistently reliable data on the vortex structure. On the other hand, the strong unsteadiness of the core flow and the small vortex core dimension mitigate against the use of anything but global, non-intrusive measuring techniques. For these reasons we use the PIV technique in this work for measuring the velocity field in trailing vortices, complemented with statistical analysis of the experimental data to locate the vortex centerline and to correct the measured velocity field.

These experimental measurements will be compared to the two comprehensive existing models for trailing vortices, which are self-similar solutions to the boundary-layer-type approximation of the equations of motion and take into account the axial velocity component of the vortices, namely that of Batchelor (1964), and the one by Moore and Saffman (1973). We compare not only the radial velocity and vorticity profiles for a given cross section of the vortex, but also the downstream variation (decay) of their main features along the vortex axis. To check the PIV measurements of the velocity profiles, we use three different image processing techniques of the experimental data.

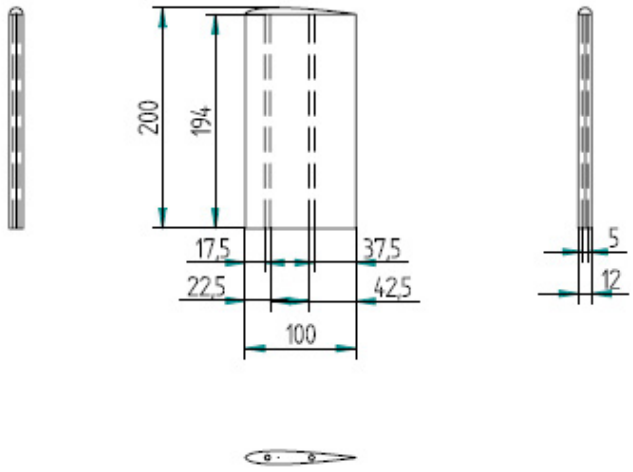

Fig. 1 NACA 0012 wing profile with a rounded tip used in the experiments. Dimensions are in mm. Shown with dashed lines are the orifices for dye injection.

2. Experimental setup

The experiments were performed in a large horizontal water tunnel in the Laboratory of Aero-Hydrodynamics at the University of Málaga, with a working section of 0.5x0.5 m^2 cross-section and 5 m long. The designed velocity range is 0 - 0.75 m/s, which is achieved by means of two centrifugal pumps of 18.5 kW each. The flow rate is measured through a turbine flow meter located downstream of the pump which has a nominal resolution of less than 0.5%. This flow meter was

calibrated before the experiments reported below through LDA axial velocity measurements, and 2D PIV measurements on a plane parallel to the mean stream.

To generate the wing tip vortices we used a model with a NACA 0012 wing profile, with chord c=10 cm and a rounded tip (see Fig. 1). It was vertically mounted on the upper surface of the first sector of the channel working section, in such a way that the wing tip was approximately at the center of the test section. This wing model was mechanized in aluminum and painted with a special pigment to avoid or minimize corrosion by water. The wing model was attached to the upper surface of the tunnel working section through a circular window (see Fig. 2, left), especially designed and built to allow for the rotation of the wing into several positions, thus making possible the configuration of different angles of attack. In addition, this window was provided with a connection between a system of controlled injection of dye and the wing, permitting flow visualizations in the wake behind the wing tip (Fig. 2, right), which complemented the PIV measurements reported below.

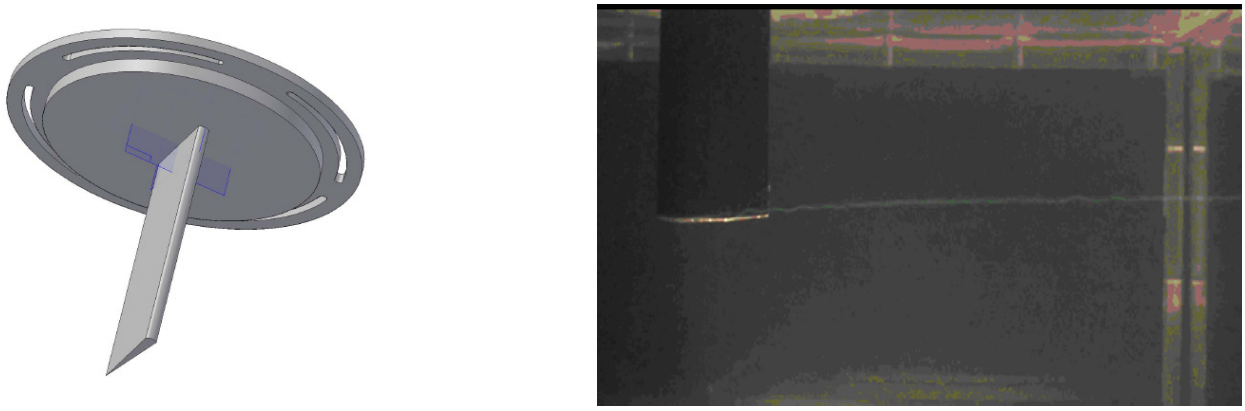

Fig. 2 Left: Illustration of the wing model attached to the circular window. Right: Photograph of the wing with a visualization of the wing tip vortex using Rhodamin 6G injected from the two small orifices of the wing tip. Angle of attack 9º and streamwise mean velocity 24 cm/s.

We used a *stereo* PIV (Particle Image Velocimetry) system for measuring the three velocity components at different cross sections of the wing tip vortex. As it is well known, the PIV technique consists on the accurate, quantitative measurement of fluid velocity vectors at a very large number of points by tracking, registering and processing the successive positions of particles inoculated into the flow (e.g., Westerveel 1997, Raffel et al 2002). Stereo PIV is used to obtain the three-component velocity field in the planar region illuminated by a laser light sheet. The fundamental principle behind Stereo PIV is the stereoscopic imaging of seed particles in an illuminated plane of the flow. Two cameras view the plane at different angles and capture particle displacement images that contain the influence of the third velocity component. Data reduction algorithms provide the true particle displacements and the on-line 3D velocity vector field display.

The stereoscopic PIV system used in this work was manufactured by the company TSI, and consists on the following elements (see Figs. 3-4): double-pulse Nd-YAG laser (150 mJ/pulse standard); 2 CCD cameras of 4MP each; light sheet optics and laser light arm; optical filter; laser pulse synchronizer, and all the auxiliary elements for mounting and aligning, and calibrating the measuring plane illuminated by the laser sheet. The particles inoculated into the flow for capturing the velocity field through the PIV system were hollow glass spheres with 10 μm diameter (HGS-10 from the company Dantec). We used the software Insight 3G-STTR for data acquisition, analysis and display (TSI 2006).

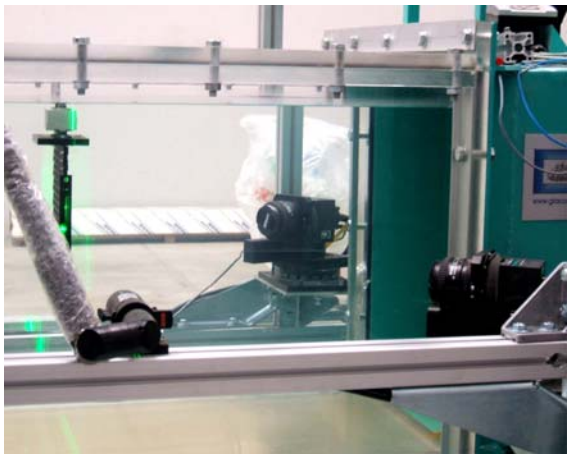

Fig. 3 Photograph showing the PIV system to measure the 3D velocity field on a test section of the tunnel. The laser sheet coming from the laser light arm illuminates the measurement plane, which is photographed by the two cameras (the wing model and the optical window are removed from the tunnel in this picture).

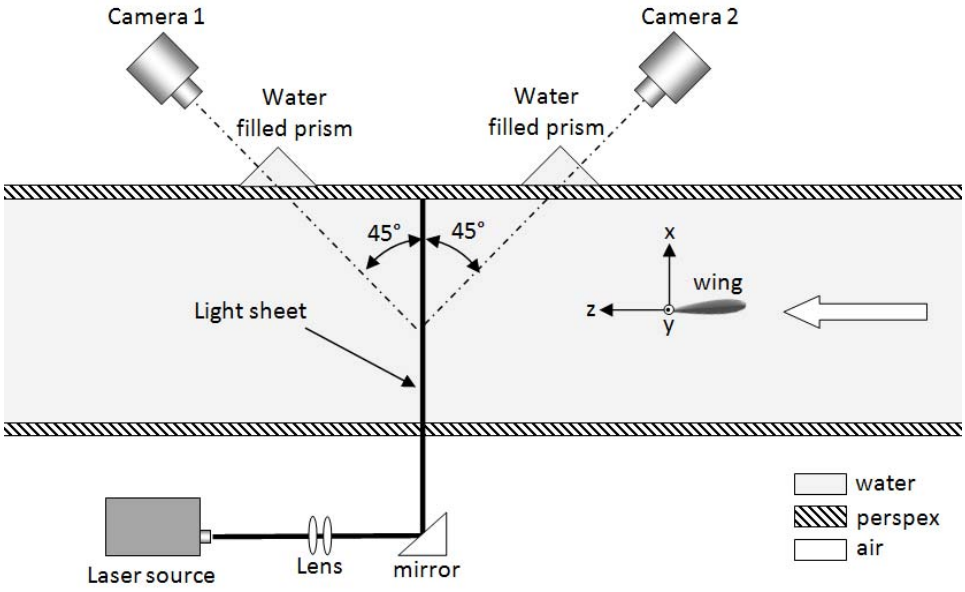

Fig. 4 Sketch of the PIV-tunnel configuration used in the 3D measurements of the velocity field. Note that both cameras are on the same lateral side of the tunnel working section.

In order to minimize the effect of refraction, two transparent (plexiglass) prismatic windows were attached to the lateral sides of the channel working section (see Fig. 4). These windows, which face normally the cameras by forming an angle of 45º with the plexiglass walls of the channel, were filled with water and adjusted through a watertight union to the channel walls.

We adopted a configuration of the PIV system in which both cameras recorded forwardly scattered light emitted from the PIV particles in the measuring plane (see Fig. 4). The intensity of forward scatter light is much larger than that from backward scatter (Raffel et al 2002), and with this configuration we obtained much better results than with the configuration shown in Fig. 3, in which each camera is on a different side of the working section, that was the first one that we tested.

3. Experimental results

We have measured the three-dimensional velocity field on cross flow planes (i.e. x-y planes, see Fig. 4) located at 6 different axial distances downstream the wing tip: z/c=0.5, 3, 4, 6, 12.5, and 16.

Tests were performed for three different angles of attack (i.e., α=6º, 9º, and 12º), and for two different flow rates (Q = 38 and 83 l/s) or Reynolds numbers. The different values of the parameters are summarized in Fig. 5. The Reynolds number is defined as Re=V c/ν, where V=Q/A is the mean velocity, with Q the flow rate and A the area of the test section of the tunnel, c is the wing chord and ν the kinematic viscosity of water. The error bars in the Reynolds number [Fig. 5(b)] take into account not only the fluctuations in the measured flow rate [Fig. 5(a)], but also those associated to the measured temperature through the kinematic viscosity, which is computed using and experimental relation for the kinematic viscosity of water given in White (2005).

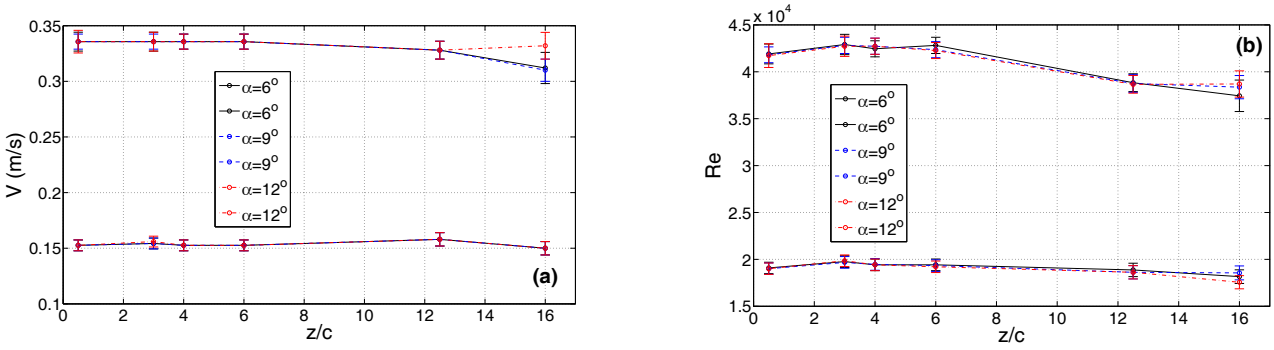

Fig. 5 Measured mean upstream velocity V=Q/A (a), and corresponding Reynolds number Re=V c/ν (b), for the different axial distances z/c and angles of attack α considered.

The parameters used for capturing images with the stereo PIV cameras were the following: PIV exposure 510 μs, laser pulse delay 425 μs, and δt = 600 μs.

3.1 PIV data processing

The determination of the three velocity components in the measurement plane required the processing of the images captured by the left and the right cameras. In order to be confident with the resulting 3D velocity fields measured with the stereo PIV system, here we used three different tools for the processing of the digital images in a number of cases, and then we compared the different results. Specifically, the following image processing algorithms were considered: i) the commercial software Insight 3G by TSI (TSI 2006) (referred to as Imag. Proc. I hereinafter); ii) an improved version of the software developed by Meunier and Leweke (2003), checked to be very effective for measuring the 2D velocity field of vortices by Meunier et al (2005, 2008), which we adapted to stereo PIV (referred to as Imag. Proc. II), and iii) the software developed by Di Florio et al. (2002) (referred to as Imag. Proc. III). For the sake of conciseness, just a general description of the adopted algorithms will be reported hereinafter, referring to the specific literature (e.g. Meunier and Leweke 2003, Di Florio et al 2002, Stanislas et al 2005) for a more comprehensive and in-depth discussion on the procedures, the uncertainty and the accuracy aspects.

The three processing softwares implement both the window off-set correlation (Westerveel 1997) and the window deformation (Scarano 2002) techniques. The former is based on a recursive processing method based on a hierarchical approach in which both the sampling grid and the size of the interrogation windows are reduced step by step during the iteration. Here, we used a two-step offset correlation with final window of 64x64 pixels. The resulting number of seed particles present in each interrogation window was around 15-20, on average. In the last iteration of the image processing techniques II and III, the interrogation windows were also 50% overlapped in order to increase the spatial resolution and, thus, to obtain a better reconstruction of the whole flow field.

We considered this approach useful especially in the tip vortex region, where the occurrence of strong velocity gradients requires an adequate resolution to be accurately resolved. In addition, this procedure has the added capability of applying interrogation windows with size smaller than the particle image displacement, increasing both the dynamic range and the spatial resolution of the measure.

	Imag. Proc. I	**Imag. Proc. II**	**Imag. Proc. III**
Iterations	2	2	2
IW size (final) [px]	64 x 64	64 x 64	64 x 64
Overlapping	0	50%	50%
Window deformation	yes	yes	yes
Image pre-processing	no	no	yes

Table 1 Image processing parameters.

A flow-adaptive-local-window-refinement-scheme was used at the end of the iterative process to shrink the interrogation windows according to the local curvature of the velocity components. This method provides a significant improvement of the PIV analysis since the image deformation reduces the number of lost of pairs statistically, the interrogation windows being deformed and adapted to the local flow direction. An in-depth description of the technique is described in Scarano (2002). The parameters used for the image processing are reported in Table1.

As an example of the 2D-PIV processing quality, Fig. 6 shows the instantaneous two-dimensional velocity fields as they were computed from the couple of images captured by the left and right cameras, respectively, using the Imag. Proc I.

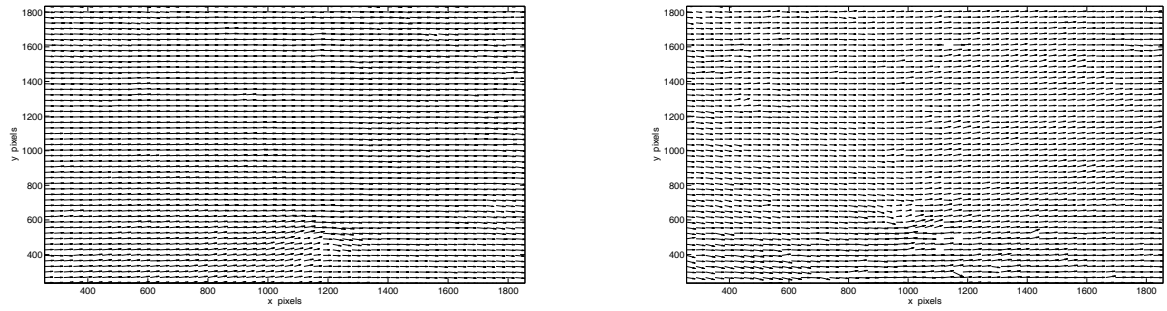

Fig. 6 Instantaneous 2D velocity fields (arrows) for Q = 83 l/s and α = 12º on the plane z/c=3 as they are processed by the software Insight 3G (Imag. Proc. I) from the two images captured from the left camera (left), and right camera (right). The plane coordinates (x,y) are in pixels of the cameras.

In the imag. Proc. III, each image was also pre-processed before the analysis. This was performed subtracting the grey scale levels of the mean image, calculated over the acquired image population. Figure 7 shows the effect of the pre-processing technique on the snapshots captured from the left and right cameras.

Each vector field was validated though a procedure that allowed detecting and replacing spurious displacement values. In this regard, we used the following validation criteria: i) the local median-filtering method (Westerveel 1997); ii) the cross-correlation signal-to-noise ratio validation (Keane and Adrian 1992); iii) the displacement range validation; iv) the geometric validation.

Stereo-reconstruction was carried out using the technique described by Soloff et al (1997). In this

regard, camera views were calibrated using a special target with a mesh of 20x20 dots in two planes. This allowed determining the transfer function by which the distribution of the three-velocity components was obtained from the two separate 2D-PIV measurements. In addition, this non-linear transformation allowed taking into account the optical distortions introduced by the presence of multiple interfaces (air, plexiglass and water), besides the geometrical correction of the perspective. The measurement area, defined as the overlapping region between the separate views of the left and right cameras, was about 115 mm x 80 mm. An example of the instantaneous distribution of the velocity and the vorticity fields is documented in Fig. 8 for the case of the Imag. Proc. III.

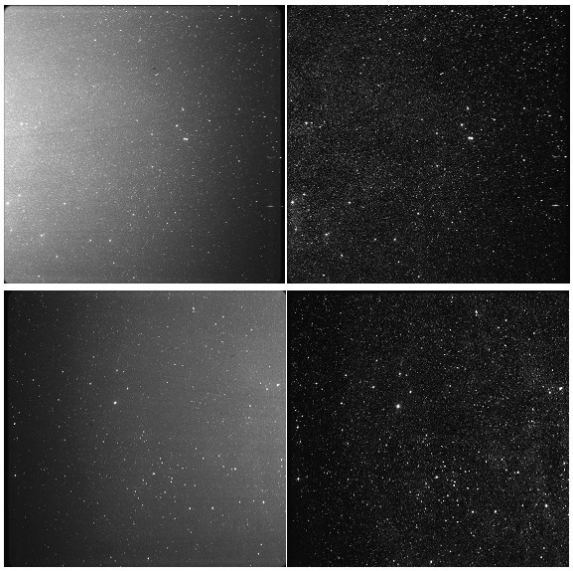

Fig. 7 Pre-processing of the images from the left (top row) and right (bottom row) cameras: original images (left), pre-processed images (right). It corresponds to an instant of time for z/c=3, Q=83 l/s, and α=12º.

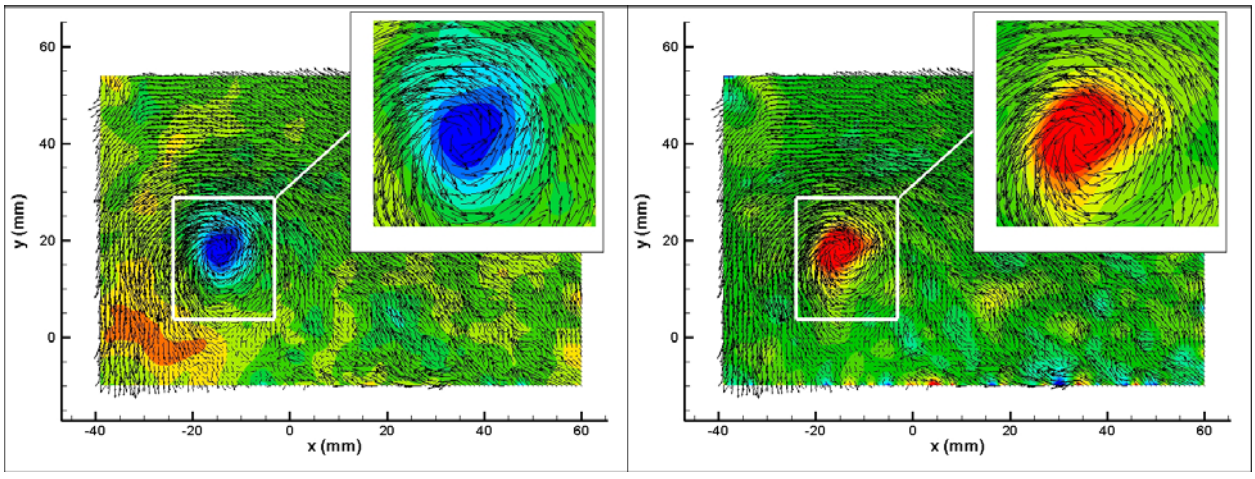

Fig.8 Left: 3D velocity field (iso-contours and vectors represent the out-of-plane and the cross-flow components respectively) on the plane z/c=3 as it is processed by the software III. Right: the same cross flow superimposed to the vorticity field in a color map (Q=83 l/s, and α=12º).

For a given case, the statistical analysis on the tip vortex was performed on a population of 450 instantaneous fields. The next step was to center the (x,y) coordinates of each one of these images at

the vortex center, which is identified as the point where the vorticity is a maximum, and, then, to average the velocity and vorticity fields using all the valid images taken for a given configuration (for given values of α, Q, and z). In this regard, Fig. 9 documents the instantaneous profiles of the axial and azimuthal velocity components and the axial vorticity at y=5.72 mm, which approximately coincides with the center of the vortex before centering in the present case. Note that the maximum in the vorticity profile is very appropriate to compute the center of the vortex at a given instant of time.

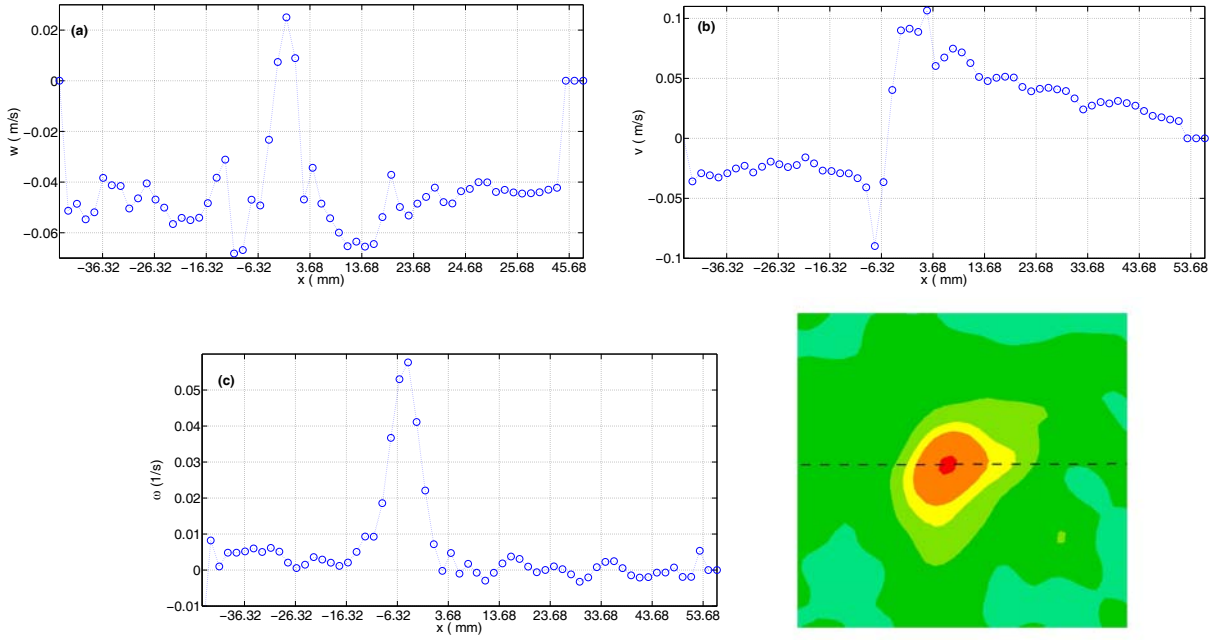

Fig. 9 Instantaneous profiles along x of the axial velocity component (top-left), the azimuthal velocity component (top-right), and the axial vorticity (bottom-left), at y=5.72 mm for the same case of Fig. 6. Profiles were extracted along the dashed line passing through the position where the vorticity is maximum (bottom-right).

For the averaging process we used a kernel of 2x2 cm^2 around the vortex axis. This re-centering and averaging process was made with a Matlab-based software and it is essential to obtain a mean velocity field that filters out the meandering phenomenon on a given plane normal to the vortex axis, such as the present one z/c=3. To avoid border effects, we discarded those images where the corresponding vortex center (maximum vorticity) was located at a distance less than 2 cm from the boundaries of the image. This method has proven to be very effective for measuring the 2D velocity field of vortices (Roy and Leweke 2005).

We averaged all the instantaneous velocity and vorticity profiles, previously re-centered using the maximum of vorticity, for a given configuration using the aforementioned procedure. Figure 10 shows these averaged velocity and vorticity fields for the same case plotted in Fig. 9. It is observed that the mean vorticity field becomes nicely concentrated around the vortex axis.

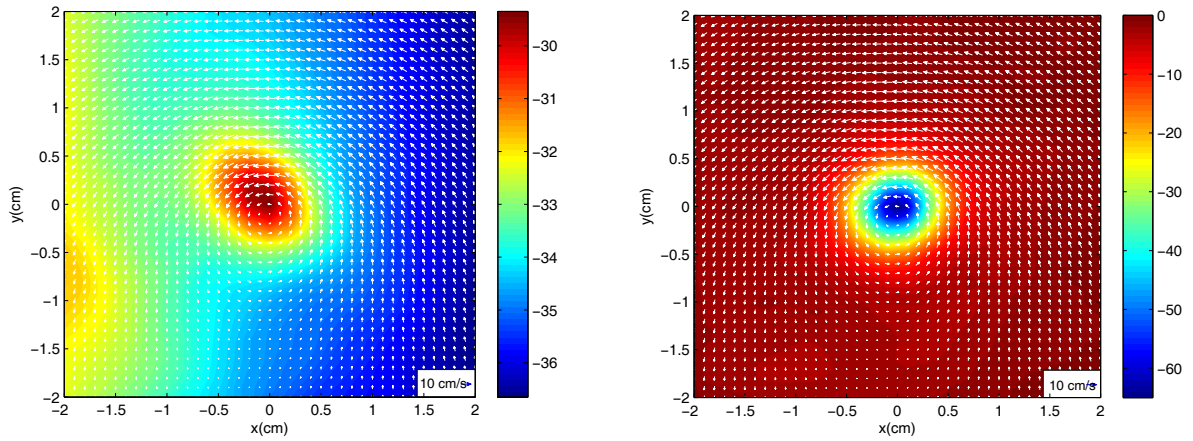

Fig. 10 Averaged and centered axial velocity (left) and vorticity (right) fields corresponding to the same configuration of Figs. 8-9.

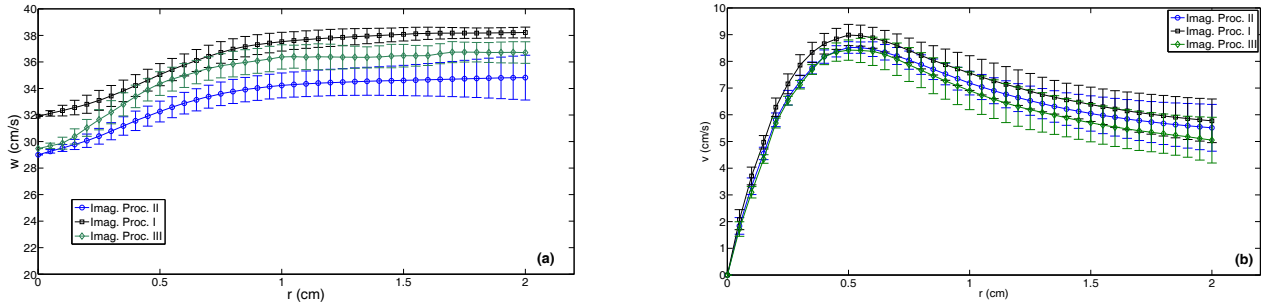

Fig. 11 Averaged radial profiles and error bars of the axial velocity w (a), and azimuthal velocity v (b), as they are obtained from the three different image processing techniques described in the text (as indicated in the legend), for z/c=3, Re =4.27 x10^4 and α = 12º.

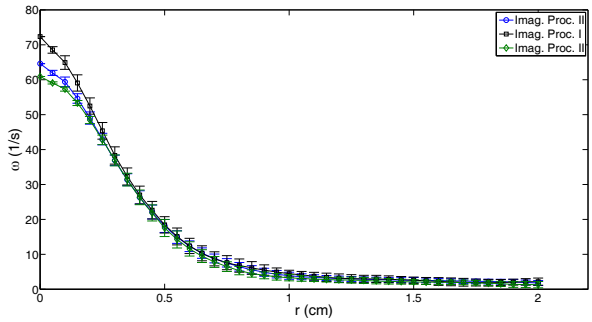

Fig. 12 Averaged radial profile and errors bars of the vorticity ω, obtained from the three different image processing techniques for the same case of Fig. 11.

3.2 Mean velocity and vorticity profiles

The mean velocity and vorticity profiles, together with their corresponding errors bars, obtained for the present case from the three image processing techniques discussed above, are given and compared in Figs. 11-12. It is observed that the mean azimuthal velocity and mean vorticity profiles are very similar, within the experimental errors. This result was corroborated for other cases whose PIV images were processed with the three techniques. Since the most relevant information for the fitting of the experimental data to the theoretical models comes from the azimuthal velocity and vorticity profiles (see below), the close agreement between the three different techniques makes us

confident about the subsequent comparison with the models using any of the three image processing techniques, especially taking into account that the most elaborate image processing technique by Di Florio et al (2002) yields practically the same mean results than the other two image processing techniques. For the comparison of the axial velocity component we shall use the averaged experimental data with image preprocessing (Imag. Tech. III), or those obtained with Imag. Proc. II, which are in close agreement, but not those obtained with the Insight 3G software (Imag. Proc. I).

It must be noted that the large errors bars in the radial profiles of both the axial and azimuthal velocity components (Fig. 11) is an indication not only of the fluctuations of the instantaneous velocity fields, but also of the non-axisymmetry of the flow, which is smoothed out in the process of computing vorticity (see Fig. 12). This is the reason why the vorticity profiles are preferred in section 4 below for fitting to the experimental results the parameters of the different theoretical models.

4. Comparison with trailing vortex models and conclusions

We compared the PIV experimental results with the two models for laminar trailing vortices that include the axial flow and are (approximate) solutions to the equations of motion, namely the model of Batchelor (1964) and that of Moore and Saffman (1973). As mentioned above, vorticity is the best fluid magnitude for fitting the experimental results to the models, since the dispersion in the experimental data is much smaller. Figure 13 shows such a comparison for the same case considered in the preceding section (note that for the comparison with the models we use non-dimensional magnitudes). It is clear that the self-similar solution of Moore and Saffman (MS) fits much better to the experimental data than the one by Batchelor (B). This is so for all the cases considered, and it was expected because Batchelor's model is valid only very far downstream from the wing tip, while Moore and Saffman's model may be valid even a few chords downstream.

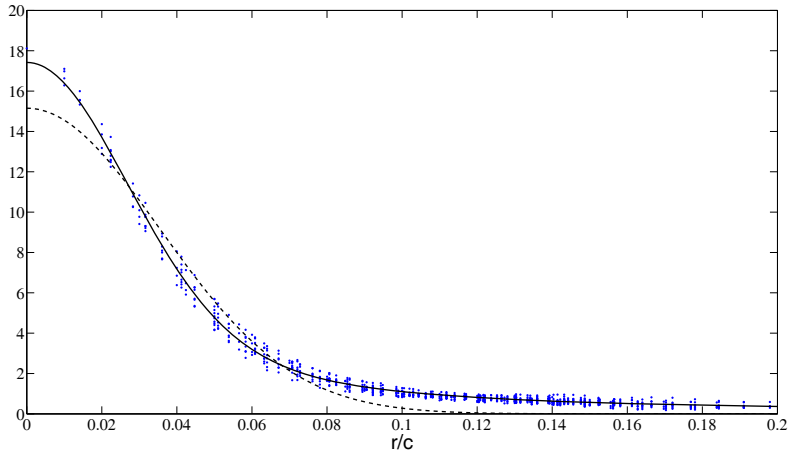

Fig. 13 Comparison between the averaged radial profile of the non-dimensional experimental vorticity (dots) with the models by Batchelor (dashed line) and by Moore and Saffman (continuous line) for z/c=3, Re =4.27×10^4 and $\alpha = 12^o$. The non-dimensional vorticity is $\omega c/V$.

Moore and Saffman's self-similar solution not only fits reasonably well, when the appropriate parameters are selected, to the radial vorticity and velocity profiles at a given plane normal to the vortex axis, but also, and this is even more relevant for adopting a wing tip vortex model, the downstream evolution of the mean velocity field. For instance, Fig. 14 shows the comparison of the non-dimensional radius where the azimuthal velocity reaches its maximum (i.e., the vortex core size) along the non-dimensional axial coordinate $\underline{z} = z/cRe$. According to both models, this radius

growths as $\underline{z}^{1/2}$, independently of the Reynolds number and the vortex strength. The fitting of the experimental values is much better to the MS model than to the B model, reaching the appropriate behavior already for $\underline{z} \sim 2\ x10^{-4}$, which corresponds to about 4 chords for $Re \sim 2\ x10^{4}$. Note that we used the power n=0.5 in the MS model considered in that figure, which is close to all the experimentally fitted values for the radial profiles measured at the maximum distance considered, i.e. z/c=16.

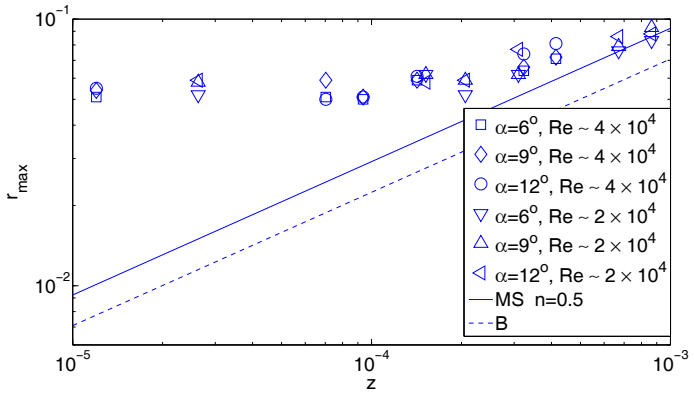

Fig. 14 Non-dimensional radius where the azimuthal velocity reaches a maximum vs. non-dimensional axial coordinate ($\underline{z}$=z/cRe) obtained experimentally for all the cases considered (as indicated in the legend), and their comparison with the models of Batchelor (B) and that by Moore and Saffman (MS) for n=0.5.

We may thus conclude that the self-similar solution by Moore and Saffman (1973) may be useful to model the structure of wing tip vortices a few chords downstream, and to predict through hydrodynamic stability analyses the dynamics and the decay of trailing vortices, provided that the Reynolds number is not too high. The use of Batchelor's vortex, or its cruder q-vortex version, which are commonly used for the stability analyses of trailing vortices, is not justified.

References

Allen A, Breitsamter C (2009) Experimental investigation of counter-rotating four vortex aircraft wake. Aerospace Sci and Tech 13:114-129.

Baker GR, Barker SJ, Bofah KK, Saffman PG (1974) Laser anemometer measurements of trailing vortices in water. J Fluid Mech 65:325.

Batchelor GK (1964) Axial flow in trailing line vortices. J Fluid Mech 20:645-658.

Deniau H, Nybelen L (2010) Strategy for spatial simulation of co-rotating vortices. Int J Num Meth Fluids 61:23-56.

Devenport WJ, Rife MC, Liapis SI, Follin GJ (1996) The structure and development of a wing-tip vortex. J Fluid Mech, 312:67-106.

Di Florio D, Di Felice F, Romano GP (2001) Windowing and deformation of PIV images for the investigation of flow with large velocity gradients. In Proc. 4th International Symposium on Particle Image Velocimetry. Götingen, Germany.

Di Florio D, Di Felice F, Romano GP (2002) Windowing, re-shaping and re-orientation interrogation windows in particle image velocimetry for the investigation of shear flows. Meas Sci Technol 13:953-962.

Fabre D, Jacquin L (2004a) Short-wave cooperative instabilities in representative aircraft vortices. Phys Fluids 16:1366-1378.

Fabre D, Jacquin L (2004b) Viscous instabilities in trailing vortices at large swirl numbers. J Fluid Mech 500:239-262.

Fabre D, Le Dizès S (2008) Viscous and inviscid centre modes in vortices: the vicinity of the neutral curves. J Fluid Mech 603:1-38.

Fabre D, Fontane F, Brancher P, Le Dizès S, Roy C, Leweke T, Fernandez-Feria R, Parras L, del Pino C (2008) Syntesis on vortex meandering. Technical Report D.1.1.1, STREP project no. AST4-CT-2005-012238, Fundamental research on aircraft wake phenomena (FAR-Wake).

Fontane J, Brancher P, Fabre D (2008) Stochastic forcing of the Lamb-Oseen vortex. J Fluid Mech 613:233-254.

Gertz Th, Holzapfel F, Darracq D (2002) Commercial aircraft wake vortices. Prog Aero Sci 38:181-208.

Gertz Th, Holzapfel F, Bryant B, Kopp F, Frech M, Tafferner A, Winckelmans G (2005) Research towards a wake-vortex advisory system for optimal aircraft spacing. Comptes Rendus Physique 6:501-523.

Huang HT, Fielder HF, Wang JJ (1993) Limitation and improvement of PIV; Part II: Particle image distortion, a novel technique. Exp Fluids 15:263-273.

Iungo SK, Skiner P, Buresti G (2009) Correction of wandering smoothing effects on static measurements of a wing-tip vortex. Exp Fluids 46:435-452.

Jacquin L, Fabre D, Gefroy P, Coustols E (2001) The properties of a transport aircraft wake in the extended near field: an experimental study. AIAA Paper 2001-1038.

Keane RD, Adrian RJ (1992) Theory of cross-correlation analysis of PIV images. Appl Sci Res 49:191-215.

Le Dizès S, Fabre D (2007) Large-Reynolds-number asymptotic analysis of viscous centre modes in vortices. J Fluid Mech 585:153-180.

Meunier P, Eloy C, Lagrange R, Nadal F (2008) A rotating fluid cylinder subject to weak precession. J Fluid Mech 599:405-440.

Meunier P, Le Dizes S, Leweke T (2005) Physics of vortex merging. C R Phys 6:431-450.

Meunier P, Leweke T (2003) Analysis and minimization of errors due to high gradients in particle image velocimetry. Exp Fluids 35:408-421.

Moore DW, Saffman PG (1973) Axial flow in laminar trailing vortices. Proc R Soc Lond A 333:491-508.

Olsen JH (1971) Results of trailing vortex studies in a towing tank. In: Aircraft wake turbulence and its detection. Plenum Press, New York, 445.

Parras L, Fernandez-Feria R (2007) Spatial stability and the onset of absolute instability of Batchelor vortex for high swirl numbers. J Fluid Mech 583:27-43.

Raffel R, Willert C, Kompenhans J (2002) Particle image velocimetry: A practical guide. Springer, Berlin, second edition.

Roy C, Leweke T (2005) Experiments on the dynamics and stability of vortex pairs with axial core flow at high reynolds numbers. In: Proceedings of the International Conference on High Reynolds Number Vortex Interactions, Toulouse, France.

Scarano F (2002) Iterative image deformation methods in PIV. Meas Sci Technol 13:1-19.

Soloff SM, Adrian RJ, Liu ZC (1997) Distortion compensation for generalized stereoscopic particle image velocimetry. Meas Sci Technol 8:1441-1454.

Spalart P (1998) Airplane trailing vortices. Ann Rev Fluid Mech 30:107-138.

Stanislas M, Okamoto K, Käler CJ, Westerweel J (2005) Main results of the Second International PIV Challenge. Exp Fluids 39:170-191.

TSI Inc. (2006) TSI Insight 3G software manual.

Westerveel J (1997) Fundamentals of digital particle image velocimetry. Meas Sci Technol 8:1379-1392.

White FM (2005) Fluid mechanics. McGraw-Hill, New York, fifth edition.

Acknowledgements. This work has been supported by the Junta de Andalucía (Spain) Grant No. P05-TEP-170.